

In the format provided by the authors and unedited.

O₂ solubility in Martian near-surface environments and implications for aerobic life

Vlada Stamenković ^{1,2*}, Lewis M. Ward^{2,3}, Michael Mischna¹ and Woodward W. Fischer²

¹Jet Propulsion Laboratory, California Institute of Technology, Pasadena, CA, USA. ²Division of Geological and Planetary Sciences, California Institute of Technology, Pasadena, CA, USA. ³Harvard University, Cambridge, MA, USA. *e-mail: Vlada.Stamenkovic@jpl.nasa.gov

1 ***Supplementary Information (SI)***

2 **O₂ solubility in Martian near-surface environments and implications for aerobic life**

3 *Vlada Stamenković^{1,3}, Lewis M. Ward^{2,3}, Michael Mischna¹, & Woodward W. Fischer¹.*

4

5 *¹Jet Propulsion Laboratory, California Institute of Technology, Pasadena, CA 91109 USA.*

6 *²Harvard University, Cambridge, MA 02139 USA.*

7 *³Division of Geological and Planetary Sciences, California Institute of Technology,*

8 *Pasadena, CA 91125 USA.*

9

10 In this Supplementary Information section, we derive all equations used in the main
11 article and give an extended discussion of our Methods. It is organized as follows. First,
12 we derive all needed equations. We then provide additional evidence for the validity of our
13 solubility and climate models. Following this, we explain why the averaging method we
14 employ for computing O₂ solubilities as a function of the annually averaged local values
15 for surface temperature and pressure is practical, and underestimates O₂ solubilities and the
16 difference between minimum and maximum values. Last, we elaborate on the implications
17 for habitability and potential extant life on Mars, and on how pressure and temperature
18 control solubility, and possibly oxidation, gradients across the Martian surface and shallow
19 subsurface (from here on termed “*near-surface*”).

20

21 **1. Detailed derivation of all necessary equations**

22 To compute the solubility of O₂ in pure water $[\widetilde{O}_2]_{aq,w}(T, P)$ in mol kg⁻¹, we start with
23 the equilibrium constant, $k(T, P)$, for a given total atmospheric pressure, P , and

24 temperature, T , which is defined for an activity coefficient of dissolved O_2 , α , and the
 25 fugacity coefficient, φ , of O_2 in the gas phase¹⁴, with VMR_{O_2} being the volume mixing ratio
 26 of O_2 in the atmosphere and the partial pressure of O_2 being $p_{O_2} = P \cdot VMR_{O_2}$

$$27 \quad k(T, P) = \frac{\alpha \cdot [\widetilde{O}_2]_{aq,w}(T, P)}{\varphi \cdot VMR_{O_2}}. \quad (8)$$

28 For Mars, we assume this value to be constant and equal to $VMR_{O_2} = 0.00145^5$. We
 29 discuss diurnal, seasonal, obliquity-driven, and atmospheric collapse-related changes in the
 30 O_2 mixing ratio in Section 2.2.5 and show that it does not affect our results. Both the
 31 activity coefficient of dissolved O_2 as well as the fugacity of O_2 in the gas phase are close
 32 to unity because of the small concentrations of dissolved O_2 and the small O_2 partial
 33 pressures that are relevant to our study (independent of temperature, for $[\widetilde{O}_2]_{aq,w} \rightarrow 0$ and
 34 $P \rightarrow 0$, the definitions for activity coefficient and fugacity demand that $\alpha \rightarrow 1$ and $\varphi \rightarrow 1$,
 35 respectively¹⁴). Therefore, Equation 8 simplifies to

$$36 \quad k(T, P) = \frac{[\widetilde{O}_2]_{aq,w}(T, P)}{VMR_{O_2}}. \quad (9)$$

37 To compute the solubility $[\widetilde{O}_2]_{aq,w}(T, P)$, we need to compute the equilibrium
 38 constant, $k(T, P)$, which is defined by the change in molar Gibbs potential
 39 $\Delta G^*(T, P)$ between the dissolved and gaseous phases¹⁴

$$40 \quad k(T, P) = \exp\left(\frac{-\Delta G^*(T, P)}{RT}\right). \quad (10)$$

41 $R = 8.3144598 \text{ J mol}^{-1} \text{ K}^{-1}$ is the universal gas constant. We compute the molar
 42 Gibbs potential through the chemical potential $\mu(T, P)$ for both the dissolved (μ_{aq,w,O_2})
 43 and gaseous (μ_{g,O_2}) O_2 phases

44 $G^*(T, P) = \left(\frac{\partial G}{\partial N}\right)_{T, P} = \mu(T, P),$ (11)

45 and, hence, $\Delta G^*(T, P) = \mu_{aq, w, O_2}(T, P) - \mu_{g, O_2}(T, P)$. Note that the chemical potential is
 46 a function of both temperature, T , and pressure, P . In order to compute the solubility of O_2
 47 in water, we need to know the chemical potential of O_2 in the gaseous and dissolved
 48 aqueous phases as a function of temperature and pressure.

49 We refer to Equations 10-11, where the chemical potential is defined through the
 50 molar Gibbs potential, in order to compute $\mu(T, P)$ in relation to a reference
 51 state, $\mu(T_{ref}, P_{ref})$, by calculating the differential $d\mu(T, P)$ from (T_{ref}, P_{ref}) to (T, P)
 52 using the entropy, S , the internal energy, U , and the molar volume, V , for both phases

53 $d\mu(T, P) = dG^*(T, P) = d(U + PV - TS) = dU + VdP + PdV - TdS - SdT.$ (12)

54 With the definition of the internal heat

55 $dU \equiv \delta Q - PdV,$ (13)

56 and the definition for the entropy

57 $dS \equiv \frac{\delta Q}{T},$ (14)

58 we obtain

59 $d\mu(T, P) = \delta Q - PdV + VdP + PdV - TdS - SdT = VdP - SdT.$ (15)

60 Therefore, we can rewrite the chemical potential as

61
$$\mu(T, P) = \mu(T_{ref}, P_{ref}) + \int_{P_{ref}}^P VdP' - \int_{T_{ref}}^T S(T')dT'. \quad (16)$$

62 The entropy, S , is a function of temperature and can be related to the specific heat at
 63 constant pressure, $C_p(T)$, which is more useful (experimentally directly measurable) than
 64 the entropy itself, with Equation 14 and $\delta Q|_P = C_p dT$ we get

$$\begin{aligned}
65 \quad S(T) &= S(T_{ref}) + \int_{T_{ref}}^T dS \\
66 \quad &= S(T_{ref}) + \int_{T_{ref}}^T \frac{C_P(T')}{T'} dT' + \overbrace{C_P(T) - C_P(T)}^{=0} \\
67 \quad &= S(T_{ref}) - C_P(T) + \frac{\partial}{\partial T} \left(T \int_{T_{ref}}^T \frac{C_P(T')}{T'} dT' \right). \quad (17)
\end{aligned}$$

68 Therefore, we replace in Equation 16 the integral over the entropy and obtain in
69 Equation 18 the chemical potential at temperature, T , and reference pressure, P_{ref} , which
70 corresponds to the temperature-dependent function in Equation 2 from our Methods

$$\begin{aligned}
71 \quad \tilde{\mu}(T) &= \mu(T, P_{ref}) \quad (18) \\
72 \quad &= \tilde{\mu}(T_{ref}) - S(T_{ref}) \cdot [T - T_{ref}] + \int_{T_{ref}}^T C_P(T') dT' - T \int_{T_{ref}}^T \frac{C_P(T')}{T'} dT'.
\end{aligned}$$

73 To fully solve for the chemical potential, we need to consider effects by pressure,
74 described by $\int_{P_{ref}}^P V dP'$ in Equation 16. For the gas phase (hence, for $\mu_{g,O_2}(T, P)$), we
75 assume an ideal gas with $PV = RT$ (for one mol) and, hence,

$$76 \quad \int_{P_{ref}}^P V dP' \Big|_g = RT \ln \left(\frac{P}{P_{ref}} \right). \quad (19)$$

77 For the dissolved phase, we assume that the molar volume of dissolved O_2 , V_{aq,O_2} , is
78 smaller than that of water, V_w , and, hence, we get $V_{aq,O_2} = \lambda V_w$ with $0 < \lambda < 1$. Using this
79 volume estimate with the standard molar volume for water at reference temperature and
80 pressure of $V_w(T_{ref}, P_{ref}) = 1.8 \cdot 10^{-5} m^3 mol^{-1}$ (water is approximately incompressible

81 for the pressures and temperatures at which we are interested), we find that $\int_{P_{ref}}^P V_{aq,O_2} dP'$
82 is negligible and would, if included, only increase the solubility of O_2 by about 0.1%.
83 Therefore, from relationships in Equations 9-11, 16, 18-19, we obtain Equation 20

$$84 \quad [\widetilde{O}_2]_{aq,w}(T, P) = \frac{p_{O_2}}{P_{ref}} \exp\left(\frac{\tilde{\mu}_{g,O_2}(T) - \tilde{\mu}_{aq,w,O_2}(T)}{RT}\right), \quad (20)$$

85 which corresponds to Equation 1 in our Methods Section (compare also with other
86 sources^{1,3,4}). Note that the pressure dependence derived here corresponds to Henry's law.

87 From here, to compute $\tilde{\mu}_{g,O_2}(T) - \tilde{\mu}_{aq,w,O_2}(T)$, we need standard values at
88 (T_{ref}, P_{ref}) for the chemical potentials and entropy of gaseous and dissolved O_2 and the
89 specific heat of O_2 in the gas phase, $C_{P,O_2,g}(T)$, and dissolved in pure water, $C_{P,O_2,aq}(T)$, as
90 a function of temperature. Experiments⁶ confirm that $C_{P,O_2,g}(T) = C_{P,O_2,g}(T_{ref})$; all
91 parameters at reference conditions can be found in Table S1.

92 We examine the choice for the specific heat of dissolved O_2 in pure water and the
93 effects of salts on the solubility of O_2 in the following section and associated subsections.

94

95 **2. Extended evidence for the validity of methods**

96 **2.1. Solubility model**

97 In the next subsections, we discuss our solubility model in greater detail.

98

99 ***2.1.1. Specific heat of dissolved O_2 and solubility – tests and robustness of results***

100 Experiments show $C_{P,O_2,aq}(T)$ increases slightly as temperature decreases from 373-
101 273 K, with no data available below this temperature range¹³. There is reason to expect that
102 the trend of increasing heat capacity continues from 273 K down to ~225-235 K but

103 possibly also below this limit. Such a steep increase of $C_{P,O_2,aq}(T)$ is justified by arguing
 104 that the behavior of the specific heat of water at cooler temperatures below ~ 300 K directly
 105 corresponds to the behavior of the specific heat capacity of dissolved O_2 . This assumption
 106 can be partially rationalized, as the smooth increase in the specific heat of pure water from
 107 300 K into the supercooled water domain down to ~ 225 - 235 K can be explained by stronger
 108 hydrogen bonds at lower temperature¹, and, hence, a greater amount of heat being needed
 109 in order to increase the ambient temperature. This increase in hydrogen bonding for lower
 110 temperatures is expected to similarly affect the dissolved O_2 , which will be partially
 111 polarized due to the water dipoles, leading potentially to a similar behaviour of the specific
 112 heats of water and dissolved O_2 below 273 K. However, thermodynamics demands that
 113 $\lim_{T \rightarrow 0 K} C_P = 0$. Indeed, some theoretical predictions find that the specific heat of
 114 supercooled water could start to decrease again for $T \sim 225$ - 235 K, where potentially a
 115 liquid-liquid phase transition could occur⁹. We emphasize that experiments to date also
 116 allow for the heat capacity to continue increasing into much cooler regions below 235 K.

117 We use for our nominal best estimate (BE) the simplest assumption that $C_{P,O_2,aq}(T) =$
 118 $C_{P,O_2,aq}(T_{ref})$, but we also test other reasonable forms of $C_{P,O_2,aq}(T)$ (all show a similar
 119 result), and derive a thermodynamic worst case, which technically cannot be reached –
 120 assuming the validity of Equations 1-2 from our Methods Section.

121 Assuming $\left(\frac{C_{P,O_2,aq}}{C_{P,w}} \sim const. \right)$ below 273 K (so that the specific heat of dissolved O_2
 122 scales with the specific heat of water), and taking the predicted specific heat behavior⁹ of
 123 supercooled water – consisting of an initial power law increase below 273 K towards a
 124 critical temperature, T_{crit} , of 225-235 K, below which the heat capacity exponentially decays
 125 towards 0 K, we find that at 140 K, O_2 solubility values are within 20% of our best estimate

126 (BE). Therefore, if the specific heat of dissolved O_2 behaves similar to the theoretical
127 predictions for the specific heat of supercooled water, then our best estimate is an excellent
128 prediction for the solubility of O_2 below 273 K.

129 Alternatively, we examine what happens if we assume that, instead, the specific heat
130 of dissolved O_2 in water behaves similar to the specific heat of a “normal fluid” that does
131 not show anomalous behaviour like water, such as a very salty NaCl brine⁹. For NaCl-
132 brines⁹ and many other brines including perchlorates¹⁰, the specific heat is rather constant
133 but does decay slowly with decreasing temperature. Assuming an unusually strong linear
134 decrease of $C_{P,O_2,aq}(T)$ by 50% from 293 to 140 K (a few factors to ~ 1 order of magnitude
135 larger than generally found for very salty brines^{9,10}), we obtain values for the solubility of
136 O_2 at 140 K that are ~ 3 times lower than our best estimate. Thus, we conclude that, for all
137 reasonable forms of $C_{P,O_2,aq}(T)$, the solubility values at 140 K are generally similar to the
138 best estimate assuming a constant heat capacity for dissolved O_2 in pure water. In the next
139 section, we derive a thermodynamic lower bound that cannot be reached as our
140 conservative worst-case scenario.

141

142 **2.1.2. Specific heat of dissolved O_2 and thermodynamic worst case (WC)**

143 The solubility of O_2 in mol m^{-3} in pure water or brine depends on the specific heat of
144 dissolved O_2 , $C_{P,O_2,aq}$, in the following way (see Equations 1 and 3 in Methods Section, and
145 Equations 18 and 20 here in the SI)

$$146 [O_2]_{aq}(T, \zeta(T)) = F(T) \exp\left(\frac{\zeta(T)}{RT}\right),$$

$$147 \text{ with } \zeta(T) = - \int_{T_{ref}}^T C_P(T') dT' + T \int_{T_{ref}}^T \frac{C_P(T')}{T'} dT' . \quad (21)$$

148 The function $\zeta(T)$ contains all the uncertainties introduced by the behavior of
 149 $C_{P,O_2,aq}(T)$, whereas $F(T)$ depends only on well-constrained properties, and
 150 monotonically increases for lower temperatures. We develop a thermodynamic lower limit
 151 for $\zeta(T)$, which gives a lower limit for the solubility of O_2 in supercooled water. To achieve
 152 this, we need to assess the behaviour of $\zeta(T)$.

153 First, we show that $\zeta(T_1) > \zeta(T_2): \forall(T_1 < T_2)$, so, independent of the temperature
 154 dependence of the heat capacity, solubilities monotonically increase for lower temperatures,
 155 with the minimum solubility curve for $T < T_{min}$ given by

$$156 [O_2]_{aq}(T, \zeta(T)) > [O_2]_{aq}(T) \Big|_{min} = [O_2]_{aq}(T, \zeta^*) \text{ with } \zeta^*(T) = \zeta(T = T_{min}), \quad (22)$$

157 where T_{min} is the lowest temperature above which we know $C_{P,O_2,aq}(T)$ sufficiently
 158 well. The most conservative worst-case estimate assumes that $T_{min} = 273 \text{ K}$ because we
 159 have data on $C_{P,O_2,aq}(T)$ above 273 K; we make this our conservative worst case that is
 160 used as the ‘‘WC’’ scenario in the main article.

161 Equation 22 is derived in the following way: $\forall T: T > 0, C_P(T) > 0$, and $T_{ref} > T$ we
 162 have $T' > T$ and therefore $\frac{T}{T'} < 1$. Hence, we can establish the following relationships

$$163 \left\| T \int_{T_{ref}}^T \frac{C_P(T')}{T'} dT' \right\| < \left\| \int_{T_{ref}}^T C_P(T') dT' \right\| \quad (23)$$

$$164 \int_{T_{ref}}^T C_P(T') dT' < 0 \text{ and } \int_{T_{ref}}^T \frac{C_P(T')}{T'} dT' < 0. \quad (24)$$

165 Therefore, we conclude that

$$166 \zeta(T) = - \int_{T_{ref}}^T C_P(T') dT' + T \int_{T_{ref}}^T \frac{C_P(T')}{T'} dT' > 0, \forall(T, C_P(T)). \quad (25)$$

167 Next, to $\zeta(T)$ being a positive function, based on Equations 23-25, $\zeta(T)$ also
 168 monotonically increases for lower T because:

">0" as shown in Eq.25

$$\zeta(T_1) = \zeta(T_2) - \overbrace{\int_{T_2}^{T_1} C_P(T') dT'} + T_1 \int_{T_2}^{T_1} \frac{C_P(T')}{T'} dT' > \zeta(T_2), \forall (T_1 < T_2). \quad (26)$$

170 Finally, with Equation 26, we have a full proof for Equation 22. Our worst case (WC)
 171 assuming Equation 22 and $T_{min} = 273 \text{ K}$ provides the logic for a conservative lowermost
 172 bound on O_2 solubility, and it is important to note that the true solution is likely to be much
 173 greater and closer to our best estimate (BE) scenario. This is because our WC solution
 174 indirectly implies that $C_{P,\text{O}_2,\text{aq}}(T) = 0$ already for $T < T_{min} = 273 \text{ K}$ but
 175 thermodynamics teaches us that this limit of $C_{P,\text{O}_2,\text{aq}}(T) = 0$ can only occur at $T = 0 \text{ K}$.
 176 Compare in Fig. S1 how our worst case is only slightly greater (20 % at 140 K) than a
 177 solubility curve assuming $C_{P,\text{O}_2,\text{aq}}(T) = 0$ for all temperatures. Please note that we could
 178 also reasonably choose $T_{min} = 225 \text{ K}$, where supercooled water is suspected to have a
 179 turning point for the specific heat to start declining for smaller temperatures°. In that case,
 180 our solution would follow from 298 K the BE scenario until 225 K instead to just 273 K
 181 and would assume $C_{P,\text{O}_2,\text{aq}}(T) = 0$ for $T < 225 \text{ K}$. This would lead to a
 182 significant additional increase in O_2 solubility curve in comparison to our conservative
 183 worst case estimate with $T_{min} = 273 \text{ K}$ (see Fig. S1). Also, Section 2.1.1 describes in
 184 detail how other reasonable assumptions on $C_{P,\text{O}_2,\text{aq}}(T)$ below 273 K would lead to
 185 solubilities very close to BE.

186

187 **2.1.3. Derivation of Pitzer coefficients for perchlorates**

188 We use the experimental results¹¹⁻¹³ on the O_2 solubility in perchlorate brines containing
 189 the salts NaClO_4 , KClO_4 , RbClO_4 , and LiClO_4 to derive the Pitzer interaction coefficients

190 for the O₂-perchlorate ion interaction O₂-ClO₄⁻, described by $\lambda_{O_2-ClO_4^-}$ in Equation 4 in our
191 Methods Section. Generally, the temperature dependence of the Pitzer coefficients is
192 negligible, but we examine this in the next section. The O₂-cation interaction coefficients,
193 λ_{O_2-c} , for the cations c=(Ca²⁺, Mg²⁺) are taken from literature¹¹.

194 We show the results for the salting out coefficient, $\gamma_{O_2}(X, m_X)$, for a brine containing
195 m_X mol kg⁻¹ of salt X in Fig. S2 for chlorides and perchlorates (compare with Equation 3 in
196 our Methods Section). There are no direct data on O₂ solubility for Ca- or Mg-perchlorates
197 and, hence, there are no data on the secondary Pitzer interaction coefficients describing the
198 interactions between O₂-cation-ClO₄⁻, λ_{O_2-c-a} . However, as we explain in the Methods
199 Section, the secondary interaction coefficients are generally negative as they represent the
200 disturbance of the respective cation-O₂ and anion-O₂ fields, which drive the solubility of O₂
201 in the liquid. Any reasonable value for $\lambda_{O_2-c-a} < 0$ would only lead to a reduction of the
202 salting out factor, $\gamma_{O_2}(X, m_X)$, and would therefore result in *greater* solubilities for O₂ in
203 perchlorate brines. Thus, we assume $\lambda_{O_2-c-a} = 0$ for Ca- and Mg-perchlorate brines—and
204 accept that this approach will tend to, if anything, underestimate the solubilities for O₂ in
205 those brines.

206

207 **2.1.4. Temperature dependence of Pitzer coefficients**

208 It is commonly found that the Pitzer coefficients introduced in Equation 4 in the
209 Methods Section are only weakly temperature-dependent^{14,15} as suggested by experiments¹⁵.
210 The wide amount of experimental data that we collected and against which we test our
211 results^{11-13,15-19} suggest also a slight increase of Pitzer coefficients for lower temperatures. We
212 find that the temperature dependence of the Pitzer coefficients could lead to an additional

213 decrease of the solubility of O₂ in Ca- and Mg-perchlorate brines at 140 K by a factor of 3-
214 10 (most likely less than 5).

215 To derive this estimate, we made use of the salting out theory of Tromans³. He
216 observes that a salt reduces the solubility of O₂ by reducing the molar volume of water (that
217 is dissolving O₂) into an apparent water volume, V_{app} . He also finds that the change in
218 apparent water volume can be used to infer the salting out factor. Thus, what we do first is
219 to derive the apparent molar water volume as a function of the brine density, ρ_{brine} , molar
220 concentration, m_X , of the salt, X , with molecular mass, M_X , in kg mol⁻¹ and molecular
221 crystalline volume, V_X , and the molar mass of pure water, M_w , leading to Equation 27

$$222 \quad V_{app}(T) = \left(\frac{1 + m_X M_X}{\rho_{brine}(T)} - m_X V_X \right) M_w(T). \quad (27)$$

223 Equation 27 is easiest to derive by computing the density of the brine,
224 ρ_{brine} , assuming that water has an apparent volume, V_{app} , and that the salt preserves its
225 crystalline molecular volume, V_X , and solving for V_{app} (for values, see Table S2).

226 Second, we compute how this apparent water volume in Equation 27 changes during
227 a reduction of temperature from 298-140 K. The temperature dependence for $V_{app}(T)$
228 results from the temperature dependence of the brine density and the molar volume of water,
229 but $V_{app}(T)$ is mainly sensitive to small changes in brine density, $\rho_{brine}(T)$. Thus, to
230 compute how $V_{app}(T)$ changes with temperature, we focus solely on determining how the
231 density of a brine, $\rho_{brine}(T)$, changes with temperature when salt and molality are fixed.

232 There are no data or theoretical predictions for the temperature dependence of the
233 density of perchlorate brines. To obtain an estimate of how much the density changes for
234 Ca- and Mg-perchlorate brines with up to ~4.2 mol of salt per kg water (= 4.2 mol kg⁻¹, the

235 concentration at the eutectic for Ca-perchlorate^{10,14,20,21}, see Table S3 for values) for a
 236 temperature change from 298-140 K, we turn towards experimental data^{22,23} on the density
 237 of a range of brines of different compositions (i.e., NaCl, MgCl₂, CaCl₂, KCl, K₂SO₄, MgSO₄,
 238 and Na₂SO₄), and examine how their densities change from 373-243 K for various salt
 239 concentrations up to 30 weight % (or ~4.2 mol kg⁻¹). We observe that variations in brine
 240 density driven by temperature are rather small and would amount to less than a 5-10%
 241 increase in density from 298-140 K—assuming a linear increase of the density towards
 242 lower temperatures with a gradient determined between 303-243 K. Note, also, that our
 243 available data indicate that the density variations decrease for lower temperatures, and one
 244 obtains very similar results including data up to 373 K in order to estimate the density
 245 gradient with temperature.

246 The derivation of the density gradient is illustrated in Fig. S3a, where we plot the
 247 density gradient for diverse brines with temperature as a function of molality using density
 248 data from 303-243 K. Extrapolating these values would lead to a density increase by less
 249 than 5-10% at 140 K in comparison to 298 K (on average about 6% for a random sampling
 250 of temperature intervals between 303-243 K). Note that this compares quite well with the
 251 predicted and measured density variation of NaCl brines between 240-300 K⁹, which would
 252 lead to a 5% increase in the NaCl brine density from 298-140 K for a linear extrapolation
 253 (which most likely overshoots the density change).

254 With this approach, we use a density increase of 5-10% for a Ca(ClO₄)₂ brine from
 255 298-140 K to measure the apparent volume changes for a 4.2 mol kg⁻¹ Ca(ClO₄)₂ brine from
 256 298-140 K, $\frac{V_{app}(\varepsilon \cdot \rho_{brine})}{V_{app}(\rho_{brine})} \approx \frac{V_{app}(140 K)}{V_{app}(298 K)}$, where ε is either 1.05 or 1.1 (corresponding to the
 257 increase in brine density from 298-140 K by 5-10%). This is illustrated in Fig. S3b, where

258 we plot the change in apparent water volume as a function of standard brine density for our
259 4.2 mol kg⁻¹ Ca(ClO₄)₂ brine at 298 K. We calculate this density using Equation 27, inverting
260 for the brine density and setting $V_{app}(298 K) \approx V_w(298 K)$ as a first order approximation.
261 This leads to an estimated 4 mol kg⁻¹ Ca(ClO₄)₂ brine density at 298 of ~1440 kg m⁻³, and
262 thus values for $\frac{V_{app}(\varepsilon \cdot \rho_{brine})}{V_{app}(\rho_{brine})}$ between 0.875-0.935.

263 We then use the theory of Tromans³ that can be used to infer how a decrease in
264 apparent volume by a factor of 0.875-0.935 affects the increase in salting out coefficient.
265 Adhering to the reference KOH line of Tromans³ (see his Fig. 7 which shows how the
266 salting out factor is a function of apparent volume change), we see that a temperature
267 change from 298-140 K would maximally yield an increase in salting out factor between
268 ~3-10 (for the average value of 6% density increase from 298-140 K, it would be a factor
269 of ~5). Therefore, even if we account for a potential temperature dependence of Pitzer
270 coefficients, then we would maximally obtain dissolved O₂ concentrations at 140 K that are
271 3-10 (and likely less than ~ 5) times lower than what we observe with our best estimate
272 shown in Figs. 1-4.

273

274 ***2.1.5. Existence of perchlorate brines under Martian conditions and the importance of*** 275 ***“near-surface”***

276 For a brine at surface temperature, T , and pressure, P , to be liquid for limited amounts
277 of time the concentration of salt must correspond to the critical molality, $m_X(T)$, at this
278 temperature (see Methods Section) but the pressure must be also above the triple point
279 pressure, $P_{TP}(m_X)$, for that specific brine. For pure water, the triple point pressure is ~6.1
280 mbar, around the average atmospheric pressure on Mars. At this pressure, the melting and

281 boiling temperatures converge, which would limit the time-limited presence of liquid water
282 to temperatures close to 273 K (this explains the narrow water range in Fig. 2 for Mars).

283 For brines, however, the triple point pressure is significantly reduced. Specifically, for
284 Ca-perchlorate brines, the salt concentrations, m_X , needed for the brine to be liquid at the
285 surface temperatures obtained with our general circulation model (GCM) simulations
286 (below ~ 230 K, see Table S4) result in triple point pressures at least one order of magnitude
287 below the minimal atmospheric surface pressure of ~ 1 mbar encountered in our GCM. The
288 triple point pressure can be approximately computed as the intersection between the
289 standard “water ice-vapour” phase curve in temperature-pressure space and an isotherm
290 for a given temperature, $T_{TP} = \max(T, T_{eu})$ (with surface temperatures T ranging from
291 ~ 145 -230 K and the eutectic temperature for Ca-perchlorate brines of $T_{eu} = 198.2$ K).
292 Therefore, the pressure conditions on Mars support the studied Ca-perchlorate brines with
293 salt concentrations $m_X(T)$, which we show in Fig. 3, to be liquid for a limited amount of
294 time (atmospheric water vapour limits the time of existence, see below). Moreover, due to
295 the approximate incompressibility of water and brines between ~ 1 bar and ~ 1 mbar, we do
296 not expect any significant change in eutectic temperature from Earth to Mars surface
297 pressures.

298 Note that for remaining liquid for extended periods of time (so next to stability against
299 freezing and sublimation), the partial vapour pressure will also matter because it determines
300 the stability against evaporation. Here, we look only at the existence of brines and do hence
301 not account for additional effects by the atmospheric vapour pressure at this point in time.
302 We note however that even a thin layer of soil or regolith can effectively prevent

303 sublimation, which makes our results especially valid in the shallow subsurface—
304 exemplifying the choice of focusing on “near-surface” environments in this first study.

305

306 ***2.1.6. Comparison with Earth today***

307 It is interesting to note that the Mars-to-Earth solubility conversion factor (= solubility
308 value at the same temperature but changing from an atmosphere of 6.1 mbar with 0.145%
309 O₂ to one with 0.21 bar O₂ is ~23,742). So, if the solubility of O₂ in pure water on Mars at
310 slightly above 273.15 K is ~2·10⁻⁵ mol m⁻³, it is, at the same temperature, about 23,742
311 greater on Earth today, or around 0.47 mol m⁻³.

312 The main enhancement factor for dissolved O₂ on modern Mars is the much lower
313 surface temperature in comparison to the Earth.

314

315 **2.2. Climate model**

316 In the next subsections, we discuss our climate model in greater detail.

317

318 ***2.2.1. Albedo variation with obliquity change***

319 The albedo of the Martian surface and how it changes with obliquity can potentially
320 be a significant control on surface temperatures. For any rotating planet, annually averaged
321 insolation at the poles increases going from zero obliquity to larger values, leading to a
322 warming of cooler regions (poles) and a cooling of warmer regions (low latitudes) as
323 obliquity rises (as seen in Table S4 for annually averaged temperatures for present-day
324 Mars). For a homogenous albedo distribution across the planet’s surface, above 54°
325 obliquity, the poles receive more insolation than the equator²⁴, and become the ‘warmer’

326 regions of the planet (on an annual basis), whereas the tropics become the ‘cooler’ region
327 and, therefore, the preferred location for surface ice formation.

328 The exact timing of how surface ice on Mars evolves with changing obliquity is
329 uncertain, as is the exact distribution of tropical surface ice at high obliquity. Different
330 studies alternatively suggest that water ice will condense widely across high topographic
331 and/or high thermal inertia sites on the planet at high obliquity²⁵, or only in localized glacial
332 deposits on the flanks of the Tharsis Montes²⁶. The impact of the exact distribution on
333 surface albedo on temperature can potentially be significant. For example, during the early
334 phases of an obliquity transition (say, from lower to higher values), ice will likely remain
335 in the polar regions for some time after the obliquity rises because of the multi-kilometre
336 thickness of the polar caps. Albedo, then, may remain relatively high at the poles, while it
337 concurrently increases in the tropics due to the development of ice deposits there as
338 obliquity rises. Later in the obliquity transition, though, it is likely that the albedo at the
339 poles will decrease as a darker, dirty sublimation lag forms atop the retreating polar ice cap.
340 The timing of this transition will be gradual and difficult to model precisely.

341 We perform a series of tests of the end-member cases from previous studies^{25,26}, looking
342 at the effect of their putative ice distributions on the global surface temperatures at high
343 obliquity, looking at different stages of the aforementioned evolution, with bright ice in the
344 poles only, in both the tropics and poles, and in the tropics only. While the annually
345 averaged global surface temperature does decrease with the presence of tropical ice, (which
346 covers a larger fraction of the surface with high albedo ice than the poles at low obliquity),
347 the general trend in surface temperatures with obliquity continues regardless of the exact
348 distribution of ice. Differences in surface temperatures between the end members of surface

349 ice distribution are in the range of 5-10 K while the minimum of the annually averaged
350 surface temperature values varies by up to ~ 35 K. This behaviour is reflected in the O_2
351 solubility results in Fig. 4a where, with increasing obliquity, the maximum solubility
352 (corresponding to the lowest annually averaged temperature on the surface) generally
353 decreases.

354

355 ***2.2.2. South polar ice cap***

356 We do not impose any constraints on ice caps for our obliquity calculations; however,
357 on modern-day Mars, observations reveal a perennial polar cap of CO_2 ice in the south
358 (SPC), which global climate models cannot self-consistently reproduce without making
359 specific, ad hoc assumptions. In our GCM calculations, we set the surface temperature to
360 the pressure-dependent CO_2 frost point for all locations poleward of -85° . This GCM model
361 is listed in Table S4 as “ 25° with SPC” and represents the most realistic climate model for
362 Mars today. We use this model to study modern Mars and to create Fig. 3 in our main
363 manuscript. Mechanisms for forming such a south polar CO_2 cap are not well understood,
364 and, hence, we cannot (and do not) extrapolate it to other obliquities; therefore, we also run
365 a 25° obliquity simulation without the presence of a south polar cap, as shown in Fig. 4.
366 Fig. 4 highlights that the “with SPC” model leads to about one order of magnitude greater
367 maximum solubility values on the Martian surface today because of the fixed low
368 temperatures for the southern polar regions. The WC scenario is not much affected by the
369 specific assumptions on SPC.

370 We must emphasize that there is no reason to assume that a SPC should form at
371 different, non-modern obliquities, especially not at higher obliquities where the poles are
372 expected to be much warmer (see Table S4).

373 If we were to arbitrarily enforce a SPC at all obliquities, then this would significantly
374 reduce the secular variation of the maximum value of O₂ solubility with obliquity change.
375 This is because, at each obliquity, there would be a small region at the south pole with
376 temperatures at the pressure-dependent frost point of CO₂, which would only vary with
377 pressure changes associated with an evolving obliquity. The secular behaviour of the
378 average values of O₂ solubility would, however, not be changed by assuming an SPC at
379 each obliquity because of the small size of the SPC region. Also, as we show in Fig. 4, the
380 lowest temperatures apart from the SPC do increase with increasing obliquity as the poles
381 start to warm; thus, the highest values outside the SPC for the solubility of oxygen in brines
382 do indeed decrease significantly with obliquity, suggesting the robustness of our trends
383 independent of our SPC assumption.

384

385 ***2.2.3. Atmospheric collapse***

386 For obliquities below ~10-15°, we find that, on geological timescales, the atmosphere
387 collapses due to the presence of permanent CO₂ cold traps in the polar regions. This can be
388 seen in Table S4, where we show how the minimum value for the annually averaged surface
389 temperature is at the pressure-dependent CO₂ frost point temperature for lower obliquities.
390 This model scenario is not likely to have occurred in the last twenty million years, might
391 occur rarely in the next five million years (Fig. 4b), but might have occurred more
392 frequently in the deeper past²⁷.

393 Atmospheric collapse will, hence, not significantly affect the time period that we study,
394 but it is interesting to consider what could happen to O₂ concentrations during such an event.
395 O₂ is produced in the Martian atmosphere through photochemical reactions from CO₂ and
396 H₂O, and subsequent hydrogen escape²⁸; hence, in order to understand how O₂ reacts to
397 atmospheric collapse, we need to understand how atmospheric water and CO₂ behave
398 during an atmospheric collapse. See Section 2.2.5, where we explore in detail how the
399 mixing ratios of O₂, CO₂, and H₂O scale over different timescales.

400

401 ***2.2.4. Averaging method and extension to daily temperature variations***

402 For practical reasons, we generate climate data of annual averages of temperature and
403 pressure as a function of location on the Martian surface for various obliquities (see details
404 on climate model above). The solubility at each point on Mars' surface is evaluated for this
405 annual average of temperature and pressure. It is important to point out that by doing such
406 time-averaging, the solubility results shown in Figs. 1-4 and the differences between
407 minimum and maximum solubilities shown in Fig. 4 are lower than if we instead compute
408 the annual average of solubility as a function of hourly or daily averages.

409 With our averaging approach, we underestimate the solubility because $[O_2]_{aq}$
410 increases exponentially towards 0 K, hence the gradient $\left| \frac{\partial [O_2]_{aq}}{\partial T} \right|$ is greater for lower
411 temperatures and the solubility evaluated at the average annual temperature is lower than
412 the solubility averaged over a greater time (and, hence, temperature) interval. The solubility
413 is linear in pressure and, thus, using the annually averaged pressure does represent the
414 precise average for the solubility as a function of pressure. Computing the annual average
415 of the O₂ solubility directly from the non-averaged temperature (daily or hourly) would

416 only increase our O₂ solubility estimates and strengthen the conclusions.

417

418 ***2.2.5. Variation in the Mars O₂ mixing ratio and timescales of interest***

419 We assume a constant mixing ratio of O₂, in agreement with currently published
420 measurements^{5,29-31}. To explore the validity and possible limitations of this assumption, let
421 us briefly revisit how O₂ forms in the Martian atmosphere: CO₂ is the major component in
422 the Martian atmosphere (volume mixing ratio of ~0.96)⁵. CO₂, being photolyzed by solar
423 UV radiation below 2275 Å ($2\text{CO}_2 + \text{UV} \rightarrow 2\text{CO} + \text{O}_2$), is the major source of O₂^{28,32-33},
424 with a photochemical lifetime for O₂ of ~30 years³⁴. Without catalysts, the recombination
425 of CO and O to CO₂ is much slower than the combination of two O atoms to form O₂, and
426 it is primarily (amongst other factors like the temperature dependence of the CO₂ cross
427 section²⁸) the existence of odd hydrogen species (HO_x, which are mainly formed by the
428 photolysis of water vapour) that catalyse the recombination of CO and O into CO₂,
429 allowing the Martian atmosphere to predominantly consist of CO₂ and have only trace
430 amounts of O₂, with a modern O₂ mixing ratio of ~0.145%⁵.

431 We would expect that the abundance of O₂ is primarily linked to the abundance of
432 CO₂ and H₂O in the Martian atmosphere; hence, in order to explore how the abundance
433 and the volume mixing ratio of O₂ could fluctuate over different timescales, we have to
434 first explore the variability of the abundances of CO₂ and H₂O over different timescales.

435 Here, we focus on diurnal and seasonal timescales of CO₂ and H₂O to study the
436 robustness of our O₂ solubility predictions based on annual averages for a fixed obliquity,
437 and on larger timescales in the order of thousands to millions of years that are relevant to
438 changes in obliquity²⁷ or thousands of years that are relevant to atmospheric collapse.

439 **2.2.5.1. Diurnal and seasonal variability**

440 The CO₂ and H₂O cycles on Mars reflect deposition and sublimation of both species
441 on diurnal and seasonal scales. However, as indicated by work on dry atmospheres³⁵, four
442 orders of magnitude variation in the H₂O abundance affect the O₂ mixing ratio by less than
443 a factor of three, and, hence, the diurnal and seasonal variations in water vapour, which are
444 one to two orders of magnitude³⁶, do not affect our conclusions—which suggests solubility
445 differences of many orders of magnitude over the Martian near-surface. If there is, for our
446 work, any significant variation of the O₂ mixing ratio for annually averaged maps, then this
447 could come from variations in the CO₂ abundance, which can fluctuate by 25% on modern
448 Mars on seasonal or diurnal timescales⁵. The mixing ratio of O₂ should, at first thought,
449 increase with a decrease of the CO₂ partial pressure (when CO₂ freezes) on timescales
450 much shorter than the lifetime of O₂ (hence, on seasonal or diurnal timescales). This would,
451 however, only modulate the mixing ratio of O₂ by 25%, which is much smaller than the
452 order of magnitude trends that we observe. However, there are no published data that
453 support such behaviour, which might suggest that the photochemical production rate of O₂
454 is fast enough to tightly couple the abundance ratio of CO₂ to O₂. Hence, the mixing ratio
455 of O₂, as CO₂ is the primary atmospheric component, should, for our purposes, remain
456 rather constant on seasonal timescales.

457

458 **2.2.5.2. Secular variation timescales**

459 **2.2.5.2.1. Obliquity change**

460 To infer how the solubility of O₂ could have changed in recent history, we studied
461 how climate changes for different obliquities. Such changes occur over thousands to
462 millions of years²⁷. These timescales are much greater than the lifetime of O₂ and, hence,

463 we expect that the abundance ratio of CO₂/O₂ remains constant and that the amount of O₂
464 scales with the amount of CO₂ and, approximately, to total pressure. Moreover, recent work
465 on dry planets³⁵ illustrate that many orders of magnitude changes in water vapour would
466 only slightly affect the O₂ mixing ratio. Hence, we expect the volume mixing ratio of O₂
467 to remain rather constant when looking at obliquity variations.

468

469 **2.2.5.2.2. *Atmospheric collapse***

470 We find in our calculations that, for low obliquities, atmospheric collapse can occur,
471 where CO₂ and H₂O fully freeze out. Such events do not seem likely in the timeframe that
472 we study; however, we find such events lasting thousands of years, on timescales much
473 greater than the photochemical lifetime of O₂. The first species to fully freeze out would
474 be H₂O. This could lead to a full photolytic transformation of CO₂ into CO and O₂,^{28,35}
475 with O₂ still being non-condensable at such temperatures—leading to the possibility of a
476 highly oxidizing Mars environment during such times of atmospheric collapse, which
477 might be related to observations of MnO₂ by MSL³⁷ and redox-stratified ancient lake
478 environments³⁸. Nonetheless, in the same timeframe, the CO₂ atmosphere would freeze
479 out, and, hence, to fully answer the question of what really happens to O₂ during times of
480 atmospheric collapse, one would have to study the dynamic aspects of such a transition and
481 individual duration of collapse for each species, which is beyond the scope of this paper.

482

483 **2.2.5.3. *Conclusion for assuming a constant O₂ mixing ratio***

484 Variations of the mixing ratio of O₂ have so far not been conclusively found, but if
485 they occur, then they should modulate our results only by a factor of a few, whereas our
486 geographic and obliquity-driven secular change conclusions show differences in O₂

487 solubilities by many orders of magnitude. Therefore, our assumption of a constant mixing
488 ratio for O₂ is reasonable.

489

490 **3. Life and aerobic environments**

491 **3.1. Aerobic environments versus aerobic habitats**

492 We explore Martian brines that could contain enough O₂ to be biologically relevant and
493 accessible by organisms. However, we intentionally study “aerobic environments” and not
494 “aerobic habitats”. We could well imagine an aerobic habitat (that organisms inhabit) at
495 greater depth (where it is significantly warmer) below an O₂-rich brine environment
496 accessing the stored O₂. Hence, although the aerobic environments we explore could be a
497 habitat (as we explore in greater depth in the next subsections), such O₂-rich environments
498 can be also seen as only biologically relevant—making the aerobic environments we
499 explore biologically relevant far below the not-yet-well-constrained lower temperature
500 limit for life (see Section 3.2).

501

502 **3.2. The lower temperature limit for life and the potential of aerobic habitats**

503 To answer whether the aerobic environments that we explore could be more than just
504 biologically relevant resources and, indeed, be habitats, much more work beyond the scope
505 of this paper will be required, focusing on the habitability of highly saline, likely low water
506 activity fluids, exploring not just the availability of O₂, but its fluxes and complementary
507 reducing species, and especially studying the low temperature limits to life. The question
508 of what the lower temperature limit to life is sticks out. While the temperatures for high-O₂
509 brines described here are low relative to those typical for life on Earth, no hard, lower

510 temperature limit for life has been established³⁹; metabolic activity and cell growth have
511 been observed at temperatures below -20°C ⁴⁰.

512 The lower temperature limit for life is much less constrained than the upper temperature
513 limit for life, and we have to differentiate between the lower temperature limits for survival,
514 life cycle completion (i.e., reproduction), and metabolism³⁹⁻⁴².

515 The conditions setting the lower temperature limit for life are likely intracellular
516 vitrification at low temperatures⁴¹⁻⁴², where fluids inside a cell start to behave like an
517 amorphous ice of high viscosity ($>10^{12}$ Pa s). Intracellular vitrification occurs for water on
518 the Earth around -20°C and is driven by freezing of the extracellular medium. Note,
519 however, that vitrified cells, although they cannot metabolize, do survive the vitrification
520 process⁴¹⁻⁴². However, the Martian brines that we study can absorb atmospheric O_2 exactly
521 because they can remain liquid far below the freezing point of water. As an example, the
522 freezing temperature of Ca-perchlorate brines is around 198 K (-75°C), far below -20°C .
523 In such a medium (which is not common on the much warmer Earth but should be more
524 common in cold, dry environments like the McMurdo Valleys or the Atacama Desert),
525 there would be no freezing of extracellular medium and, hence, no reason for intracellular
526 vitrification. The viscosity of the fluid would also remain rather small (which corresponds
527 to the brine not being frozen or vitrified), allowing vigorous nutrient delivery for metabolic
528 activity. The much lower freezing temperatures for Martian brines and the ability of some
529 of them to effectively supercool, even when mixed with soils, are the reasons why we study
530 such brines as materials interesting to life. Hence, the general reason for a lower
531 temperature limit for life, namely extracellular medium freezing and intracellular
532 vitrification, should occur in Martian brines at much lower temperatures than -20°C —

533 exemplifying the importance of freezing point reduction for the survival of life at much
534 lower temperatures.⁴³

535 In conclusion, if Martian life could adapt to tolerate high salt concentrations such as
536 those in the brines described here, this could lead to a lower temperature limit and access
537 to higher dissolved oxygen concentrations due to the very low freezing points and
538 additional supercooling ability of these systems.

539

540 **3.3. Aerobic habitats on Mars under warmer conditions?**

541 Temperatures above -20°C (and even above the freezing point of water) exist in the
542 Martian near-surface (compare with Figs. 1 and 2 in the main article). We know that (1) at
543 temperatures above -20°C , at least from a temperature perspective, life can survive, grow,
544 and metabolize, (2) above the freezing point of water our model has been validated with
545 experimental data, and (3) at such “warmer” temperatures (above -20°C and even above
546 the freezing point of water) our model predicts a dissolved O_2 concentration of $\sim 10^{-5}$ mol m
547 ³, well above the limits of respiration for bacteria^{44,45}. Hence, although at very low
548 temperatures the question remains open as to whether aerobic environments can be habitats,
549 we know that on modern Mars—from an O_2 availability and temperature perspective—
550 near-surface conditions exist that could enable aerobic habitats.

551

552 **4. The next steps**

553 **4.1. The path towards fluxes and redox gradients**

554 As we show in Fig. S4, it is primarily temperature and secondarily pressure that
555 determine the potential solubility of O_2 in Martian near-surface environments. The

556 geographic variations in O₂ content lead to natural gradients in concentrations across
557 environments where waters might naturally flow^{46,47}. Areas where spatial gradients (as
558 shown in Fig. S4) in O₂ solubility are largest are observed on Tharsis, across Meridiani,
559 Arabia Terra, and within the Hellas basin.

560 Next to studying the fluxes of O₂ on Mars, in order to explore the potential for aerobic
561 life, we will also have to explore, in subsequent steps, the fluxes of reducing species, as
562 life needs redox gradients in order to thrive.

563

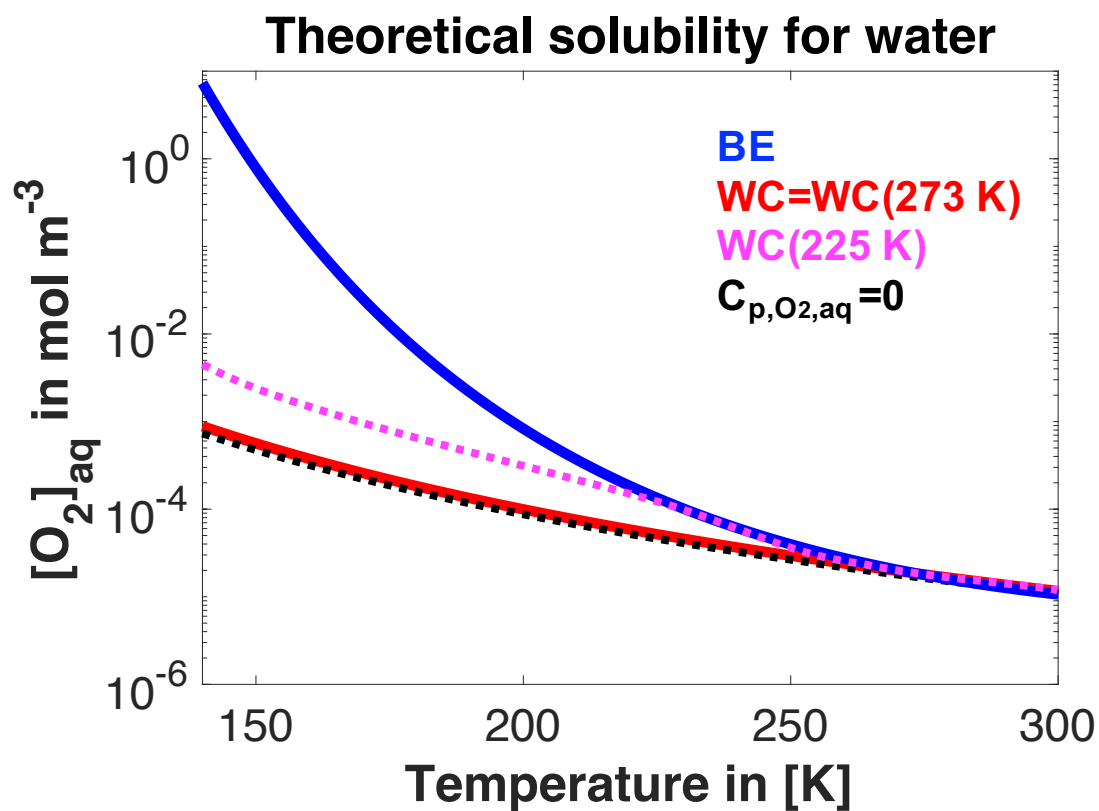
564 **4.2. Distribution, likelihood, and timescales of existence of brines on Mars**

565 The opportunity for oxidative processes involving O₂ during the chemical weathering
566 of Mars' crust will reflect a convolution between the availability of water and brines and
567 their O₂ contents. Our results suggest that we should expect a degree of patchiness in
568 oxidative chemistry associated with weathering; the same would be true for the potential
569 energetic gradients for aerobic respiration. To fully explore this patchiness, we need to
570 convolve our results with the distribution and the likelihood of brines on Mars: here, we
571 compute how climate impacts the potential for aerobic environments on Mars in 3D (Fig.
572 3), assuming that perchlorate and water are equally available everywhere close to the
573 planet's surface. Naturally, we expect spatial variability in the distribution of water and
574 perchlorates (possibly linked with each other), and, hence, as a next step, it will be
575 inevitable to explore how the distribution of perchlorates and water availability across the
576 Martian near-surface (and also deeper subsurface) might vary, how local vapour pressure
577 and soil thickness affect evaporation timescales (beyond just the potential for existence as
578 addressed here), how ice and surface features might impact the formation and longevity of

579 liquid brines close to the surface, and how these factors would affect our results.

580 Such an extension, however, demands a much deeper insight into the dynamics of
581 brine formation/destruction and gas dissolution processes (connecting subsurface and
582 atmosphere), which is beyond the scope of this first study. For the next steps of our study,
583 it would be informative to know how chlorine and hydrogen concentrations change with
584 depth in the near-surface and ultimately in the deeper subsurface. Unfortunately, currently
585 available data from the Mars Odyssey gamma ray spectrometer reach only down to a few
586 microns in depth, are strongly modulated by dust, and cannot yet see the meaningful depths
587 of the regolith that have daily or seasonal thermal cycles.

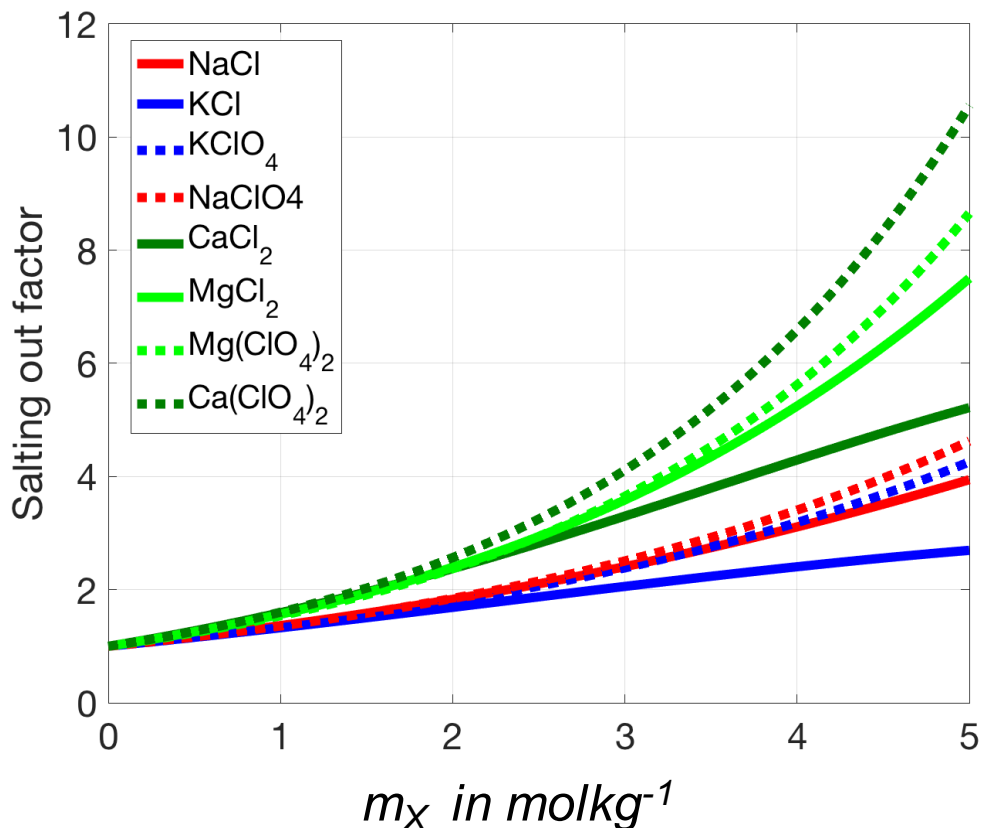
588 **Figures:**



589

590 **Fig. S1.**

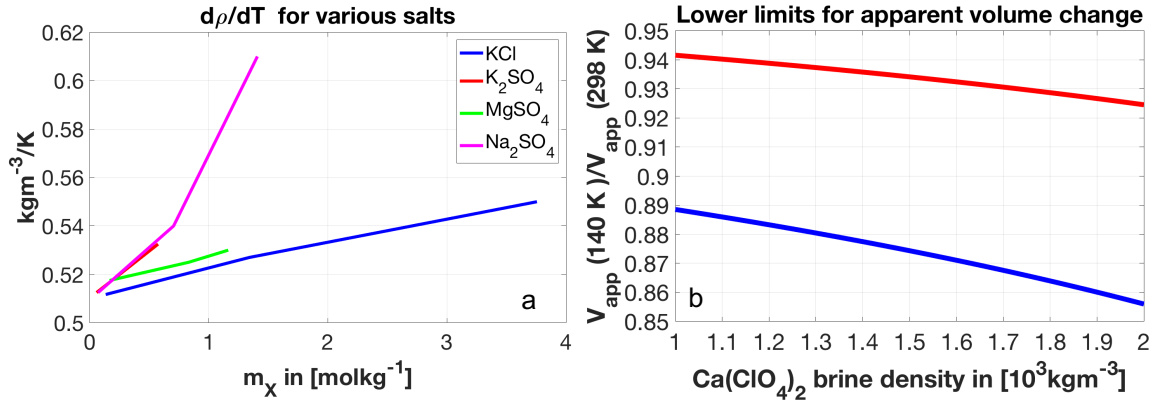
591 **Thermodynamic lower limit to the solubility of O_2 :** we compare the best estimate (BE,
592 solid blue line) for the solubility curve of O_2 in supercooled water to the thermodynamic
593 worst case (WC, solid red line), which sets the specific heat of dissolved O_2 to zero for
594 temperatures below 273 K. Formally, this is only possible for $T = 0$ K, and thus WC marks
595 a lowermost estimate. We show also a solubility curve assuming $C_{p,O_2,aq}(T) = 0$ for all
596 temperatures (black dotted line) and one assuming $C_{p,O_2,aq}(T) = 0$ for $T < 225$ K (pink
597 dotted line).



598

599 **Fig. S2.**

600 **Salting out coefficients for O_2 in perchlorate and chloride brines:** using data on the
601 solubility of O_2 in various chlorides (solid) and perchlorate (dashed) brines¹¹⁻¹³, we compute
602 Pitzer interaction coefficients at 298 K for Ca- and Mg-perchlorates, describing the salting
603 out factor, $\gamma_{O_2}(X, m_X)$, of O_2 as a function of salt concentration. We also plot the salting
604 out factors for other relevant brines (for parameters, see Table S2). $[O_2]_{aq,X}(T, P) =$
605 $\frac{1}{\gamma_{O_2}(X, m_X)} [O_2]_{aq,w}(T, P)$, wherein the salting out factor relates the solubility of O_2 in pure
606 water $[O_2]_{aq,w}(T, P)$ and in the brine $[O_2]_{aq,X}(T, P)$. The salting out factors for Mg- and
607 Ca-perchlorates are likely overestimated here, as we neglect electrostatic cation-anion- O_2
608 interactions.



609

610 **Fig. S3.**

611 **The temperature dependence of salting out factors for O_2 in various brines:** (a) the
 612 density gradient with temperature as a function of molality using density data from 303-

613 243 K. (b) Using an average density variation from 5-10% for a $\text{Ca}(\text{ClO}_4)_2$ brine, we

614 compute how the apparent volume of water changes from 298-140 K for a range of 4.2 m

615 $\text{Ca}(\text{ClO}_4)_2$ brine densities at 298 K (our estimated value is $\sim 1400 \text{ kg m}^{-3}$, see below) by

616 plotting $\frac{V_{\text{app}}(\varepsilon \cdot \rho_{\text{brine}})}{V_{\text{app}}(\rho_{\text{brine}})} \approx \frac{V_{\text{app}}(140 \text{ K})}{V_{\text{app}}(298 \text{ K})}$, where ε is either 1.05 (red) or 1.1 (blue) (representing

617 the increase in brine density from 298-140 K by 5-10%). The apparent volume depends

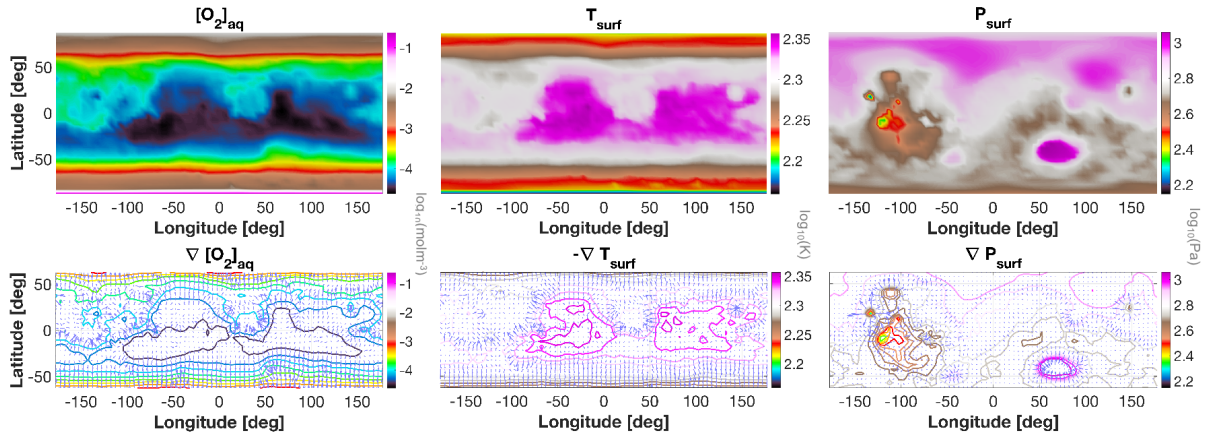
618 slightly on the reference brine density at 298 K, which we estimate by using Equation 27,

619 inverting for the brine density and setting $V_{\text{app}}(298 \text{ K}) \approx V_w(298 \text{ K})$, leading to an

620 estimated 4.2 mol kg^{-1} $\text{Ca}(\text{ClO}_4)_2$ brine density at 298 K of $\sim 1440 \text{ kg m}^{-3}$, and $\frac{V_{\text{app}}(\varepsilon \cdot \rho_{\text{brine}})}{V_{\text{app}}(\rho_{\text{brine}})}$

621 between 0.875 and 0.935. Along the KOH line in the Tromans model³, we get an increase

622 of the salting out factor between ~ 3 -10 (and likely less than a factor of ~ 5).



623

624 **Fig. S4.**

625 **The predominant factors that control O_2 solubility, and spatial O_2 solubility gradients**
 626 **on modern Mars:** this plot shows the O_2 solubilities for modern-day Mars using local
 627 annual averages for surface temperature and pressure (**top**) as well as spatial gradients
 628 (**bottom**) in O_2 solubility. The primary control on O_2 solubility is temperature and
 629 secondary modifications result from pressure.

630 **Tables:**

631 **Table S1.**

632 **Dissolved oxygen parameters:** all thermodynamic parameters needed to compute the
633 specific heat capacity for O₂ at constant pressure in the gaseous and aqueous phases,
634 essential for deriving the solubility of O₂ in pure water as a function of pressure and
635 temperature in Equations 1-2 in the Methods Section of our main article. The parameters
636 are taken from experiments. The partial volume fraction in the Martian atmosphere is
637 approximately $VMR_{O_2} = 0.00145^5$, and $R = 8.3144598 \text{ J mol}^{-1} \text{ K}^{-1}$ is the universal gas
638 constant.

Thermodynamic parameters for the solubility of O ₂ in pure water					
Phase of O ₂	$\tilde{\mu}(T_{ref})$ [J mol ⁻¹]	$S(T_{ref})$ [J K ⁻¹ mol ⁻¹]	$C_P(T_{ref})$ [J K ⁻¹ mol ⁻¹]	T_{ref} [K]	P_{ref} [Pa]
Gaseous	0	205.028	29.332	298	1.01325·10 ⁵
Aqueous	16506	109	205.266	298	1.01325·10 ⁵

639

640 **Table S2.**

641 **Salting-out and salt parameters:** specifies the ions, molality of cations (c) or anions (a)
 642 per molality of salt, the Pitzer coefficients λ^{11-13} for the interaction of O₂ molecules with
 643 cations (c), anions (a), and cations & anions (c-a), and the crystalline molar mass, M_X , and
 644 volume, V_X (values have been taken from experiments³ or computed using data²² with
 645 $V_X = M_X/\rho_X$, where ρ_X is the density at 298 K and 1 atm=1.01325 bar), for Ca(ClO₄)₂,
 646 Mg(ClO₄)₂, NaClO₄, KClO₄, MgCl₂, CaCl₂, NaCl, KCl, MgSO₄, K₂SO₄, and Na₂SO₄. The
 647 crystal data is only necessary to estimate the temperature dependence of the salting out
 648 factor.

Salting-out parameters								
Salt	Ions	f_c	f_a	λ_{O_2-c} [kg mol ⁻¹]	λ_{O_2-a} [kg mol ⁻¹]	λ_{O_2-c-a} [kg ² mol ⁻²]	M_X [kg mol ⁻¹]	V_X [10 ⁻⁶ m ³ mol ⁻¹]
Ca(ClO ₄) ₂	Ca ²⁺ /ClO ₄ ⁻	1	2	0.2497	-0.007	0	0.23898	90.147
Mg(ClO ₄) ₂	Mg ²⁺ /ClO ₄ ⁻	1	2	0.2298	-0.007	0	0.22321	101
NaClO ₄	Na ⁺ /ClO ₄ ⁻	1	1	0.1602	-0.007	0	0.12244	48.988
KClO ₄	K ⁺ /ClO ₄ ⁻	1	1	0.1519	-0.007	0	0.13855	54.980
MgCl ₂	Mg ²⁺ /Cl ⁻	1	2	0.2298	0	-0.00565	0.09521	40.81
CaCl ₂	Ca ²⁺ /Cl ⁻	1	2	0.2497	0	-0.0169	0.11098	50.5
NaCl	Na ⁺ /Cl ⁻	1	1	0.1602	0	-0.00919	0.05844	27.02
KCl	K ⁺ /Cl ⁻	1	1	0.1519	0	-0.0211	0.07455	37.52
MgSO ₄	Mg ²⁺ /SO ₄ ²⁻	1	1	0.2298	0.0878	0	0.12037	40.7
K ₂ SO ₄	K ⁺ /SO ₄ ²⁻	2	1	0.11519	0.0878	0	0.17426	65.48
Na ₂ SO ₄	Na ⁺ /SO ₄ ²⁻	2	1	0.1602	0.0878	-0.046	0.14204	53.33

649

650 **Table S3.**

651 **Eutectic curve parameters:** specifies the eutectic temperature, T_{eu} , the eutectic salt
 652 concentration, m_{eu} (in mol salt per kg water), and the parameters used to parameterize the
 653 critical concentration for the melting curve with temperature for the salts shown in Fig. 1,
 654 which are $\text{Ca}(\text{ClO}_4)_2$, $\text{Mg}(\text{ClO}_4)_2$, NaClO_4 , MgCl_2 , CaCl_2 , NaCl , and MgSO_4 . Values are taken
 655 from experimental data^{10,48}. The melting curve is defined by $m_x(T) = \sum_{i=0}^3 p_i T^i$, $T > T_{eu}$
 656 and $m_x(T) = m_{eu}$, $T \leq T_{eu}$, and determined with experimental data^{10,14,20,21,48,49}. The values for
 657 the maximal supercooling temperature, T_{sc} , are taken from available experiments²⁰.

Salt	Melting curve parameters						
	T_{eu} [K]	T_{sc} [K]	m_{eu} [mol kg ⁻¹]	p_3 [10 ⁻⁵]	p_2	p_1	p_0
Ca(ClO₄)₂	198.2	140	4.176	-1.0689	0.0069556	-1.5378	119
Mg(ClO₄)₂	209.3	140	3.375	-1.4134	0.0094903	-2.1498	167.22
NaClO₄	239.2	227.7	9.2	-0.6053	0.003012	-0.6241	69.098
MgCl₂	240.15	226.4	2.84	-8.5302	0.063718	-15.911	1330.6
CaCl₂	224	n/a	4	-2.56	0.017736	-4.1378	328.69
NaCl	251.85	245.6	5.17	0	0	-0.23877	65.22
MgSO₄	269.55	254	1.72	0	0	-0.47778	130.51

658

659 **Table S4.**

660 **Surface temperatures across obliquities:** for the simulated obliquities, the minimum,
661 average, and maximum values on the Martian globe for annually averaged surface
662 temperatures. The annotation “with SPC” is representing modern Mars, where a perennial
663 CO₂ cap at the south pole is assumed. The values [*] for obliquities of 40°, 60°, and 90°
664 represent climate simulations where the Southern Polar CO₂ cap has sublimated, doubling
665 the average surface pressure to ~12 mbar.

Temperature variation on the Martian surface with obliquity			
Obliquity [°]	Minimum annual average [K]	Global annual average [K]	Maximum annual average [K]
5	144.4	205.7	229.7
10	144.5	205.4	229.5
15	149.6	205.0	229.0
20	156.0	204.4	228.3
25	161.8	203.703	227.413
25 (with SPC)	144.2	203.651	227.389
40	172.1 [*175.7]	201.6 [*204.6]	224.1 [*226.9]
60	179.7 [*183.2]	198.0 [*201.0]	214.4 [*216.8]
90	177.2 [*179.5]	195.4 [*198.8]	208.8 [*211.9]

666

667 **Supplementary Information References**

- 668 1 Tromans, D. Temperature and pressure dependent solubility of oxygen in water: A
669 thermodynamic analysis. *Hydrometallurgy* **48**, 327-342 (1998).
- 670 2 Tromans, D. Oxygen solubility modelling in inorganic solutions: Concentration,
671 temperature and pressure effects. *Hydrometallurgy* **50**, 279–296 (1998).
- 672 3 Tromans, D. Modeling oxygen solubility in water and electrolyte solutions. *Ind. Eng. Chem.*
673 *Res.* **39**, 805-812 (2000).
- 674 4 Taylor, D. F. Thermodynamic properties of metal-water systems at elevated temperatures.
675 *Journal of The Electrochemical Society* **125**, 808, doi:10.1149/1.2131553 (1978).
- 676 5 Mahaffy, P. R. *et al.* Abundance and isotopic composition of gases in the Martian
677 atmosphere from the Curiosity rover. *Science* **341**, 263-266, doi:10.1126/science.1237966
678 (2013).
- 679 6 Chase, M. W. J. *et al.* in *Standard Reference Data Program* Vol. 1.0 (National Institute
680 of Standards and Technology, Gaithersburg, MD 20899, 1986).
- 681 7 Holten, V., Palmer, J. C., Poole, P. H., Debenedetti, P. G. & Anisimov, M. A. Two-state
682 thermodynamics of the ST2 model for supercooled water. *J. Chem. Phys.* **140**, 104502,
683 doi:10.1063/1.4867287 (2014).
- 684 8 Holten, V., Bertrand, C. E., Anisimov, M. A. & Sengers, J. V. Thermodynamics of
685 supercooled water. *J. Chem. Phys.* **136**, 094507, doi:10.1063/1.3690497 (2012).
- 686 9 Archer, D. G. & Carter, R. W. Thermodynamic properties of the NaCl + H₂O system. 4.
687 Heat Capacities of H₂O and NaCl(aq) in cold-stable and supercooled states. *J. Phys. Chem.*
688 *B* **104**, 8563-8584 (2000).
- 689 10 Toner, J. D. & Catling, D. C. Water activities of NaClO₄, Ca(ClO₄)₂, and Mg(ClO₄)₂ brines
690 from experimental heat capacities: Water activity >0.6 below 200 K. *Geochimica et*
691 *Cosmochimica Acta* **181**, 164-174, doi:10.1016/j.gca.2016.03.005 (2016).

- 692 11 Clegg, S. L. & Brimblecombe, P. The solubility and activity coefficient of oxygen in salt
693 solutions and brines. *Geochimica et Cosmochimica Acta* **54**, 3315-3328 (1990).
- 694 12 Konnik, E. I. Salting-out and salting-in of gaseous non-electrolytes in aqueous solutions of
695 electrolytes. *Russian Chemical Reviews* **46**, 577-588 (1977).
- 696 13 Khomutov N. E., Konnik, E. I. Solubility of oxygen in aqueous electrolyte solutions.
697 *Russian Journal of Physical Chemistry* **48** (1974).
- 698 14 Toner, J. D., Catling, D. C. & Light, B. A revised Pitzer model for low-temperature soluble
699 salt assemblages at the Phoenix site, Mars. *Geochimica et Cosmochimica Acta* **166**, 327-
700 343, doi:10.1016/j.gca.2015.06.011 (2015).
- 701 15 Silvester, L. F. & Pitzer, K. S. Thermodynamics of electrolytes. X. Enthalpy and the effect
702 of temperature on the activity coefficients. *Journal of Solution Chemistry* **7**, 327-337,
703 doi:10.1007/BF00662893 (1978).
- 704 16 Millero, F. J., Huang, F. & Laferiere, A. L. The solubility of oxygen in the major sea salts
705 and their mixtures at 25°C. *Geochimica et Cosmochimica Acta* **66**, 2349-2359,
706 doi:10.1016/s0016-7037(02)00838-4 (2002).
- 707 17 Millero, F. J. & Huang, F. Solubility of oxygen in aqueous solutions of KCl, K₂SO₄, and
708 CaCl₂ as a function of concentration and temperature. *Journal of Chemical & Engineering*
709 *Data* **48**, 1050-1054, doi:10.1021/je034031w (2003).
- 710 18 Geng, M. & Duan, Z. Prediction of oxygen solubility in pure water and brines up to high
711 temperatures and pressures. *Geochimica et Cosmochimica Acta* **74**, 5631-5640,
712 doi:10.1016/j.gca.2010.06.034 (2010).
- 713 19 Weiss, R. F. The solubility of nitrogen, oxygen and argon in water and seawater. *Deep-Sea*
714 *Research* **17**, 721-735 (1970).
- 715 20 Toner, J. D., Catling, D. C. & Light, B. The formation of supercooled brines, viscous
716 liquids, and low-temperature perchlorate glasses in aqueous solutions relevant to Mars.
717 *Icarus* **233**, 36-47, doi:10.1016/j.icarus.2014.01.018 (2014).

- 718 21 Toner, J. D., Catling, D. C. & Light, B. Modeling salt precipitation from brines on Mars:
719 Evaporation versus freezing origin for soil salts. *Icarus* **250**, 451-461,
720 doi:10.1016/j.icarus.2014.12.013 (2015).
- 721 22 Washburn, E. W. *International Critical Tables of Numerical Data, Physics, Chemistry and*
722 *Technology*. Vol. 3 54-95 (National Research Council, McGraw-Hill Inc., 1928).
- 723 23 Washburn, E. W. *International Critical Tables of Numerical Data, Physics, Chemistry and*
724 *Technology*. Vol. 2 327-328 (National Research Council, McGraw-Hill Inc., 1928).
- 725 24 Ward, W. R. Climatic variations on Mars: 1. Astronomical theory of insolation. *Journal of*
726 *Geophysical Research* **79**, 3375-3386, doi:10.1029/JC079i024p03375 (1974).
- 727 25 Mischna, M. A. On the orbital forcing of Martian water and CO₂ cycles: A general
728 circulation model study with simplified volatile schemes. *J. Geophys. Res.* **108**,
729 doi:10.1029/2003je002051 (2003).
- 730 26 Forget, F., Haberle, R. M., Montmessin, F., Levrard, B. & Head, J. W. Formation of
731 glaciers on Mars by atmospheric precipitation at high obliquity. *Science* **311**, 368-371
732 (2006).
- 733 27 Laskar, J. *et al.* Long term evolution and chaotic diffusion of the insolation quantities of
734 Mars. *Icarus* **170**, 343-364, doi:10.1016/j.icarus.2004.04.005 (2004).
- 735 28 Nair, H., Allen, M., Anbar, A. D., Yung, Y. L. & Clancy, R. T. A photochemical model of
736 the Martian atmosphere. *Icarus* **111**, 124-150, doi:10.1006/icar.1994.1137 (1994).
- 737 29 Barker, E. S. Detection of molecular oxygen in the Martian atmosphere. *Nature* **238**, 447-
738 448, (1972).
- 739 30 Owen, T., *et al.* The composition of the atmosphere at the surface of Mars. *J. Geophys.*
740 *Res.* **82**, 4635-4639 (1977).
- 741 31 Hartogh, P. *et al.* Herschel/HIFI observations of Mars: First detection of O₂ at submillimeter
742 wavelength and upper limits on HCl and H₂O₂. *A&A* **521**, L49, 1-5 (2010).

- 743 32 McElroy, M. B. & Donahue, T. M. Stability of the Martian atmosphere. *Science*, **177**, 986-
744 988, (1972).
- 745 33 Parkinson, T.M., & Hunten, D. M. Spectroscopy and aeronomy of O₂ on Mars. *J. Atmos.*
746 *Sci.*, **29**, 1380-1390, (1972).
- 747 34 Clancy, R.T., & Nair, H. Annual (perihelion-aphelion) cycles in the photochemical
748 behavior of the global Mars atmosphere. *J. Geophys. Res.*, **101**, E5, 12785-12790, (1996).
- 749 35 Gao, P., Hu, R., Robinson, T. D., Li, C. & Yung, Y. L. Stability of CO₂ atmospheres on
750 desiccated M dwarf exoplanets *The Astrophysical Journal* **806**, 12, doi:10.1088/0004-
751 637X/806/2/249 (2015).
- 752 36 Titov, D.V. Water vapour in the atmosphere of Mars. *Adv. Space Res.*, **29** (2), 183-191,
753 (2002).
- 754 37 Lanza, N. L., *et al.* High manganese concentrations in rocks at Gale crater, Mars. *Geophys.*
755 *Res. Lett.* **41**, 5755–5763, doi:10.1002/2014GL060329 (2014).
- 756 38 Hurowitz, J. A. Redox stratification of an ancient lake in Gale Crater Mars. *Science*, **356**,
757 eaah6849, 1-10 (2017).
- 758 39 Rothschild, L. J. & Mancinelli, R. L. Life in extreme environments. *Nature*, **409** (6823),
759 1092 (2001).
- 760 40 Bakermans, C. Determining the limits of microbial life at subzero temperatures.
761 In *Psychrophiles: From Biodiversity to Biotechnology* (pp. 21-38). Springer, Cham, (2017).
- 762 41 Clarke, A. The thermal limits to life on Earth. *International Journal of Astrobiology* **13** (2):
763 141–154, doi:10.1017/S1473550413000438 (2014).
- 764 42 Clarke, A., Morris, G. J., Fonseca, F., Murray, B. J., Acton, E. & Price, H. C. A low
765 temperature limit for life on Earth. *PLoS One*, **8**(6), e66207 (2013).
- 766 43 Chin, J. P., *et al.* Solutes determine the temperature windows for microbial survival and
767 growth. *Proc. Natl. Acad. Sci.*, **107**(17), 7835-7840, (2010).

- 768 44 Zakem, E. J. & Follows, M. J. A theoretical basis for a nanomolar critical oxygen
769 concentration. *Limnology and Oceanography* **62**, 795-805, doi:10.1002/lno.10461 (2017).
- 770 45 Stolper, D. A., Revsbech, N.P. & Canfield, D.E. Aerobic growth at nanomolar oxygen
771 concentrations. *Proc. Natl. Acad. Sci.*, *107*, 18755-18760, (2010).
- 772 46 Hanna, J. C. Hydrological modelling of the Martian crust with application to the
773 pressurization of aquifers. *J. Geophys. Res.* **110**, doi:10.1029/2004je002330 (2005).
- 774 47 Fairén, A. G. *et al.* Prime candidate sites for astrobiological exploration through the
775 hydrogeological history of Mars. *Planetary and Space Science* **53**, 1355-1375,
776 doi:10.1016/j.pss.2005.06.007 (2005).
- 777 48 Li, D. *et al.* Phase diagrams and thermochemical modelling of salt lake brine systems. II.
778 NaCl+H₂O, KCl+H₂O, MgCl₂+H₂O and CaCl₂+H₂O systems. *CALPHAD: Computer*
779 *Coupling of Phase Diagrams and Thermochemistry* **53**, 78-89,
780 doi:10.1016/j.calphad.2016.03.007 (2016).
- 781 49 Pestova, O. N., Myund, L. A., Khripun, M. K. & Prigaro, A. V. Polythermal study of the
782 systems M(ClO₄)₂-H₂O (M²⁺ = Mg²⁺, Ca²⁺, Sr²⁺, Ba²⁺). *Russian Journal of Applied*
783 *Chemistry* **78**, 409-413 (2005).